RSC Advances

ROYAL SOCIETY OF CHEMISTRY

www.rsc.org/advances

Effect of grafted amine groups on in-plane tensile properties and high temperature structural stability of borophene nanoribbons

Jianhui Yuan[ab] , L. W. Zhang[c] and K. M. Liew[*bd]

[a]*School of Physics and Electronic Science, Changsha University of Science and technology, Changsha 410114, China*
[b]*City University of Hong Kong Shenzhen Research Institute Building, Shenzhen Hi-Tech Industrial Park, Nanshan District, Shenzhen, China*
[c]*College of Information Science and Technology, Shanghai Ocean University, Shanghai 201306, China*
[d]*Department of Architecture and Civil Engineering, City University of Hong Kong, Kowloon, Hong Kong SAR*

The effects of grafted amine groups on in-plane tensile properties and structural stability of armchair and zigzag borophene nanoribbons (ABNRs and ZBNRs) are investigated by using molecular dynamics. The results show that the Young's moduli for ABNR and ZBNR are 1.093 *TPa* and 0.978 *TPa*, respectively. Their ultimate elastic strains are respectively about 15.30% and 22.03%, with showing distinct ductile and brittle fractures. When the BNRs are grafted amine groups ($-NH_2$), the moduli of ABNR and ZBNR increase to 1.125*TPa* and 1.016*Tpa*, respectively. The ultimate elastic strain for ABNR increases to 18.23% but that for ZBNR gets slightly reduced to 21.12%. The fracture modes still remain unchanged. The structural deformation after undergoing high temperature at 1500K shows that there is little difference between the ABNRs and ZBNRs, but the structural deformation for grafted BNRs is obviously less than that for non grafted BNRs. The results indicate that grafting amine groups can increase the Young's moduli, enhance the elastic strain range, reduce the in-plane elastic anisotropy and strengthen the crack resistance. In particular, grafting amine

* Corresponding author. Tel.: +852 3442 7601. E-mail address: kmliew@cityu.edu.hk (K.M. Liew).

groups can significantly strengthen their capacity to resist deformation at high temperature, reduce the thermal expansion anisotropy and improve structural stability.

1. Introduction

Two-dimensional (2D) nanosheets with atomic or molecular thickness and infinite planar lengths have attracted significant interest because of their electronic, electrical and mechanical properties.[1-3] Among them, as a 2D sheet of sp^2 conjugated atomic carbon, graphene has attracted great attention due to its specific structure and properties such as large surface area, good optical transparency, high thermal conductivity and mechanical strength.[4, 5] Graphene nanoribbons can be fabricated by lithography and can render new functionalities while preserving some of the unique properties of the pristine graphene. However, carbon's elemental near neighbour, boron, one step to the left in the Periodic Table, may muscle in on graphene's domain as the possibility of "borophene," the boron analogue of the all-carbon material, emerges from supercomputer simulations and experimental hints.[2, 6]

Over the past decade, elemental boron clusters[7-10] and the relevant low-dimensional nanostructures (fullerenes, monolayer-sheets and nanotubes, etc.)[11, 12] have been intriguing researchers working on molecular and/or nanoscale systems of interest as the elucidation of structures and bonding is the central focus. In particular, recent combined experimental and theoretical studies have led to a systematic understanding of the structural and bonding properties of small boron clusters suggesting a flat land of boron that is in stark contrast to bulk boron and boron alloys, in which three-dimensional (3D) structural units dominate.[8, 9] 2D atom-thin boron sheets have attracted increasing attention.[3] Early theoretical investigations have showed that graphene-like boron sheets with a honeycomb lattice are unstable; instead, boron tends to form buckled all triangular lattices.[13, 14] More recent theoretical studies have predicted a new type of planar boron sheets, consisting of triangular

lattices with hexagonal vacancies, which are more stable and suitable to form boron nanotubes.[15, 16] The role of the hexagonal hole has been rationalized in terms of chemical bonding.[17] Various forms of monolayer boron structures have been considered with different vacancy densities and arrangements.[18-20] The Piazza et al.[2] provide the first experimental evidence of viability of the novel boron nanostructures with hexagonal vacancies. These structures can indeed exist and may be synthesized using appropriate substrates.[21] The potential large-scale synthesis of the new atom-thick boron nanosheets calls for an appropriate name: 'borophene', in analogy with graphene. They showed that the structure of B36 is not only possible but highly stable.[2] It is one–atom thick disc with perfectly symmetrical structure and the boron atoms are arranged in a triangular lattice with a perfect hexagonal hole in the middle. Photoelectron spectroscopy revealed a relatively simple spectrum, suggesting a symmetric cluster. Neutral B36 is the smallest boron cluster to have sixfold symmetry and a perfect hexagonal vacancy that can be viewed as a potential basis for extended two-dimensional boron sheets. The electronic structure of the 2D boron sheets can be either metallic or semiconducting, according to theoretical calculations.[18, 22-24] Owing to the hexagonal holes, various chemical modifications can be made to tune the electronic and chemical properties of borophenes.[25, 26] Thus, borophene may constitute a new class of atom-thick nanostructures complementary to graphene. The borophene seems to have great potential for new applications in the near future due to abundant boron resource, light atomic weight, low mass, better economy, super strong B-B atomic bonds and special electronic structure.

In order to better understand the differences between borophenes nanoribbons (BNRs)

and their functional modifications in terms of structural stability and mechanical robustness, it is necessary to compare their basic elastic properties and structural states under high-temperature and the deforming behavior under different degrees of strain. Recently, chemical functionalization of low-dimensional carbon network systems, such as carbon nanotubes (CNTs), graphene and GNRs, by introducing molecules and groups, has attracted a lot of attention; it is being viewed as a significant way to modify their physical and chemical properties.[27-29] Some representative researches such as the effects of grafted chemical functional groups on elastic properties of CNTs, boron nitride nanotubes and graphene, and their in-plane compressive properties and thermal stability at high temperatures, etc, have been reported.[30-35] Based on these works, we further investigate the effects of grafted amine groups on armchair and zigzag BNRs (ABNRs and ZBNRs) through molecular dynamics method. The research reported in this paper mainly calculated the Young's moduli of ABNR and ZBNR with amine grafts and no grafts, optimized the geometric structures under different in-plane tensile strains and simulated the structural performance on being subjected to high temperature of 1500K. By comparing and analyzing their moduli, critical strains and structural deformation under different conditions, etc., some new results of practical value were discovered.

2. Calculation model and method

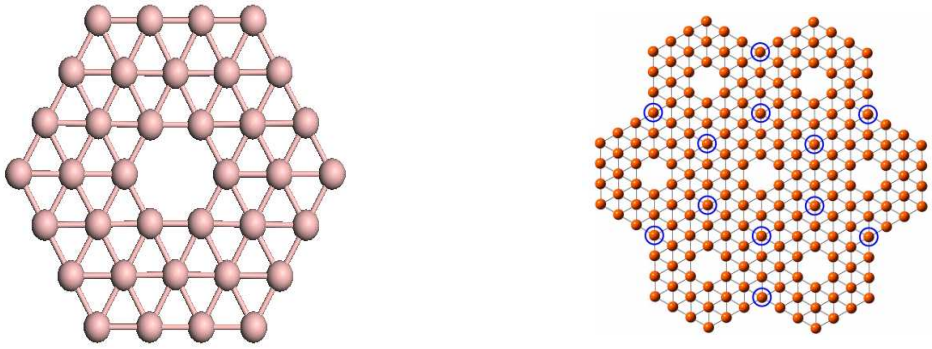

Fig. 1 Relationship between B_{36} (a) and borophene (b).

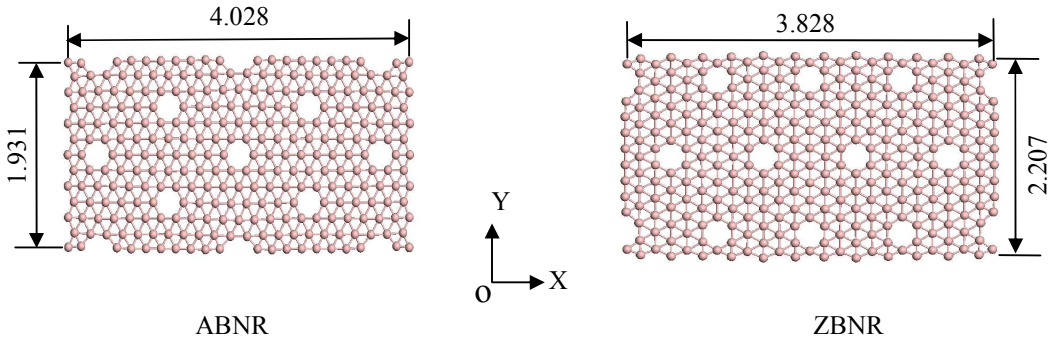

Fig. 2 Geometric models of ABNR and ZBNR (unit: nm).

As shown in Fig. 1, Borophene, constructed from the planar hexagonal B36 unit, is an extended one-atom-thick boron sheet. The B36 unit has a perfectly symmetrical structure and its boron atoms are arranged in a triangular lattice with a perfect hexagonal hole in the middle. The circles in Fig. 1b represent the apex atoms in the B36 unit, shared by three units[2]. It is one of the building blocks for boron materials in other dimensions. The BNRs (nanoribbons formed by borophene structure) can be divided into armchair and zigzag BNRs (ABNRs and ZBNRs), similar to graphene, according to the shape of the free boundary. In the simulations, ABNR and ZBNR are set up to be about the same as the model size, i.e.

4.028 nm×1.931nm and 3.828nm×2.207nm, respectively. The geometric structures are shown in Fig. 2. Because dangling bonds exist at atoms around the borders of BNR, considered to be more active, the functional groups grafted at the borders of BNR are often selected to enhance composite materials. Nitrogen and boron are easy to bond. Therefore, the functional groups grafts amine ($-NH_2$) in the simulations are considered here and they are linked symmetrically at the borders of BNR; the calculated model is shown in Fig. 3 where the functional group atom marked with an arrow is grafted to a boron atom at the borders of BNR. Finally, energy on the structures is minimised by geometry optimization. The conjugate gradient algorithm is applied to geometry optimization and the convergence thresholds for the specified maximum energy change, force, stress and displacement are set to 8.36×10^{-2} J·mol^{-1}, 4.18 J·mol^{-1}·Å^{-1}, 10^{-3} *GPa* and 10^{-5} Å, respectively. The maximum iterations of geometry optimization cycles are 10^4.

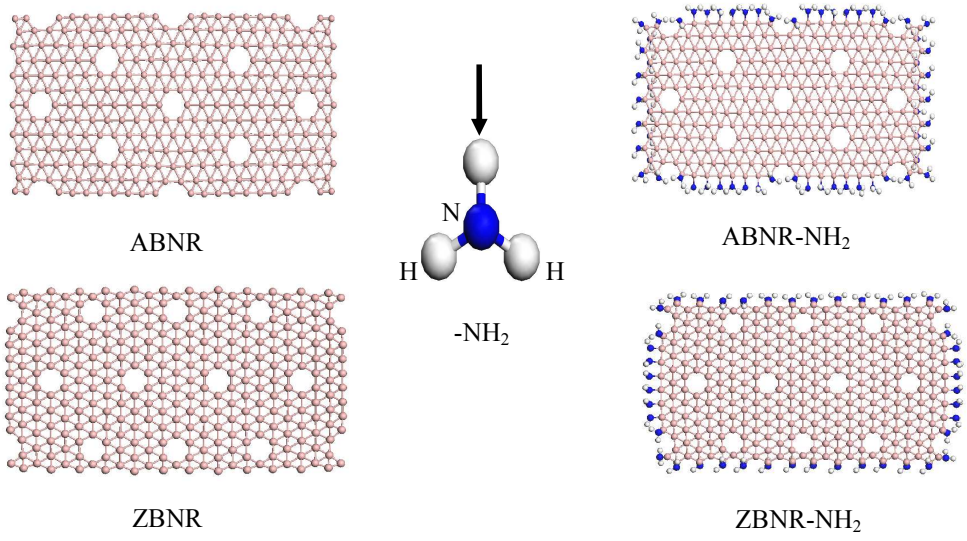

Fig. 3 Computing models of BNRs, amine grafts and their grafted structures.

According to the two types of models (Fig. 2), the procedure of the simulation is as follows. To be in line with similar previous studies,[30, 32] in simulations, the two ends of the BNR along the X direction were clamped to apply the uniform strain along x-direction and structural optimization. Because the clamped structure is not available for calculation and analysis of the system energies, a periodic boundary condition is applied in the x-direction after optimization. A free boundary is always set in the y-direction of BNR. The structures with different strain conditions are optimized and performance parameters of the optimized structures are calculated and analyzed using the universal force field (UFF).[36]

The UFF, a molecular mechanics force field, is where the force field parameters are estimated, using general rules based only on the element, hybridization and connectivity. The potential energy of the UFF is expressed as the sum of bonded and non-bonded interactions:

$$E_T = E_B + E_A + E_\tau + E_\omega + E_v + E_{el}\,. \tag{1}$$

Bonded interactions include the bond stretching E_B, the angle bending E_A, the dihedral angle torsion E_τ and the inversion terms E_ω, whereas non-bonded interactions include the van der Waals interaction E_v and the electrostatic interaction E_{el}. The UFF includes a parameter generator that calculates force field parameters by combining atomic parameters. Thus, force field parameters for any combination of different types of force fields can be generated, as required.[37-39]

The system strain energy is calculated using the UFF potential and its Young's modulus is obtained by applying the classical elasticity theory

$$Y = -\frac{1}{V_0}\frac{\partial^2 E_T}{\partial \varepsilon^2}\bigg|_{\varepsilon=0} \tag{2}$$

where function E is the total strain energy of the system, ε is the strain and V_0 is the equilibrium volume.

To ensure thermal stability, each structure was first subjected to 1000 steps (1 ps) of relaxation, followed by 10000 steps (10 ps) of stabilization at high temperature (1500 K) and thermal quenching at a rate of 300 K/ps, and finally 20000 steps (20 ps) of equilibrium after quenching to room temperature (300 K), to obtain a stable equilibrium structure. Simulations of BNRs under tensile strain can induce geometric optimization that enables atoms in the BNRs to rotate and move in relation to one another, following a certain minimization of the strain energy in a way that allows an equilibrium state to occur. Geometric structures with different strains are collected at each tensile deformation with an incremental displacement step of 0.2 Å.

3. Results and discussion

3.1. In-plane tensile properties of BNRs

Based on our computational scheme, we optimize the geometric structure of finite BNRs and BNRs-NH_2 under different in-plane tensile strains (ε), as shown in Fig. 4, 5.

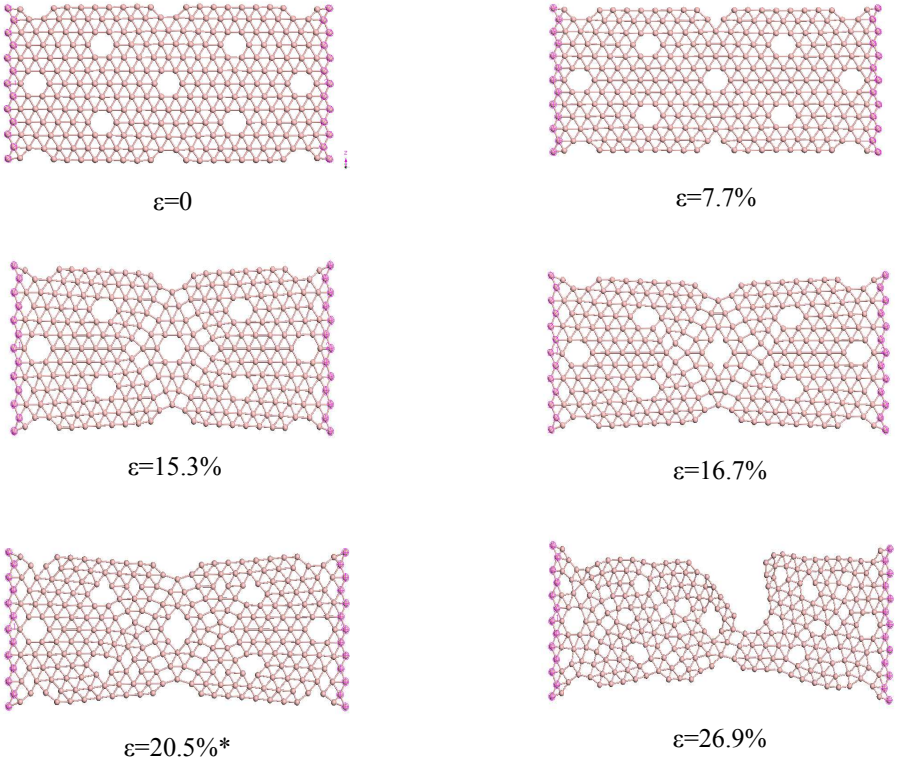

Fig. 4 Geometric structure of ABNRs with different in-plane tensile strains ε

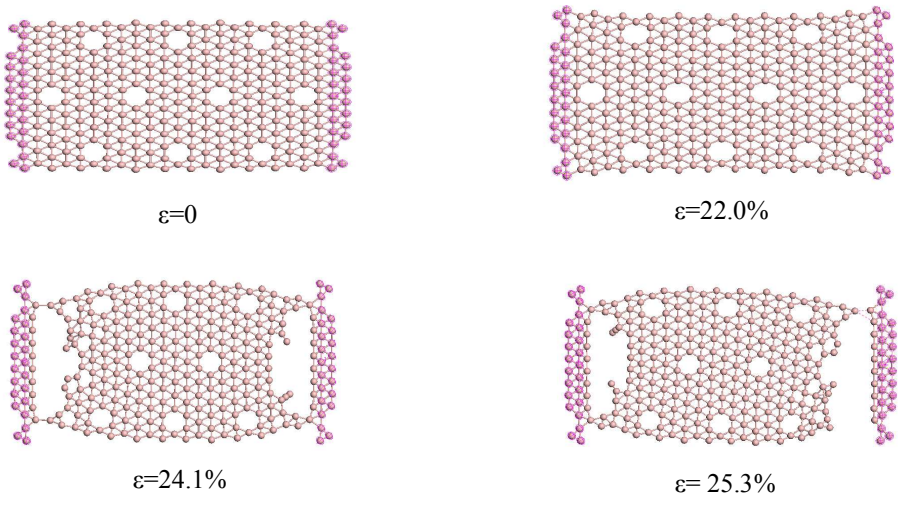

Fig. 5 Geometric structure of ZBNRs with different in-plane tensile strains ε

Fig. 4 and 5 show geometric structure changing process of ABNRs and ZBNRs. The results show that when the in-plane tensile strain reaches 7.7%, 15.3% and 16.7%, ABNR

begin to undergo cutting off, sleeking of a bond at the center of the border and internal hexagonal vacancie distortion but no distortion occurs in ZBNR until the tensile strain reaches 22.0%. In particular, when the strain reaches 26.9% and 24.1%, cracks occur in ABNR and ZBNR, respectively. The fracture modes are completely different, which shows distinct ductility for ABNR and brittleness for ZBN. The crack for ABNR begins from the middle and that for ZBNR begins from both ends. The deformations of ABNR have obvious elastic and plastic phases. The breakup for ZBNR occurs so fast that one can hardly see the transitional processes. These findings suggest that there is the planar stress anisotropy in the borophene.

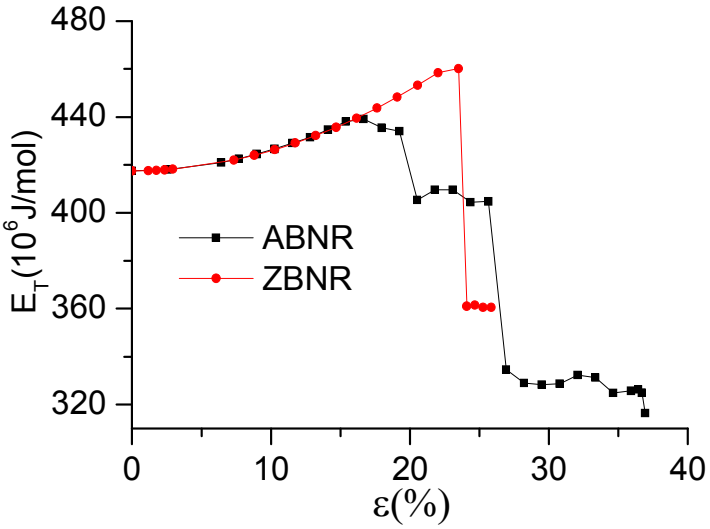

Fig. 6 Effect of different in-plane tensile strains (ε) on the total potential energy (E_T) of BNR

To deeply understand the relationship between differences in moduli of the aforementioned BNRs and their structures, we further calculated the systemic energies. Fig. 6 shows the effect of different in-plane tensile strains (ε) on the total potential energy (E_T)

of ZBNRs and ABNRs. It's easy to see that the ABNR and ZBNR have distinctly different elastic strains and slight differences in elastic modules. By fitting the curve around the equilibrium position, their elastic coefficients can be calculated. It's worth pointing out that calculating elastic modulus is meaningful only when using the thickness of the continuum assumption since the BNR membrane are composed of monolayers of boron atoms. The effective thickness of BNR is taken as 0.34nm, which is close to the distance between graphene layers in graphite crystal.[40-42] Through data fitting, the functional correlation between the total potential energy and strain around the equilibrium position can be obtained as follows:

$$E_T = 417.48365 - 0.07544\varepsilon + 869.8\varepsilon^2 \quad \text{for ABNRs} \tag{3}$$

$$E_T = 417.48529 - 0.40031\varepsilon + 845.25665\varepsilon^2 \quad \text{for ZBNRs} \tag{4}$$

Based on Formula (2), combined with Formulae (3) and (4), the Young's moduli of ABNRs and ZBNRs can be computed. The results indicate that the Young's moduli of the BNRs are generally very large, with values for ABNR and ZBNR being 1.09273 *TPa* and 0.97804 *TPa*, respectively. The Young's moduli are very close to (1.2±0.1) for zigzag and (1.0±0.1) *TPa* for armchair grapheme.[40, 43, 44] The moduli for armchair are always larger than for zigzag, while the modulus ratio of armchair to zigzag (Y_a/Y_z) is 1.117, showing that there is the anisotropy of in-plane elastic property of BNR.

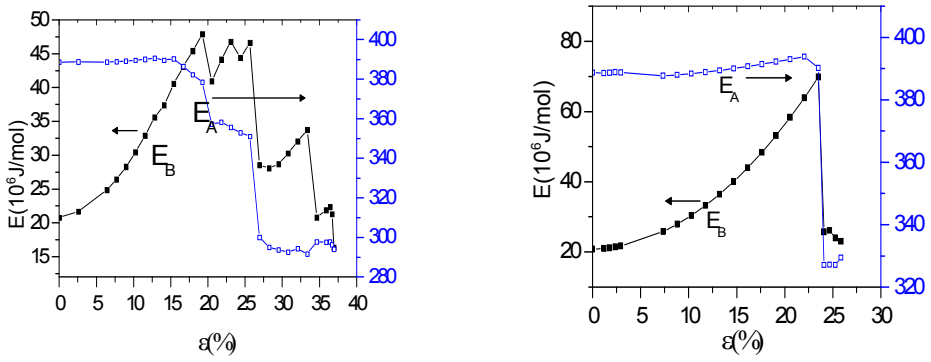

(a) ABNR (b) ZBNR

Fig. 7 Effect of different in-plane tensile strains (ε) on the bond (E_B) and angle energy (E_A) of the ABNR (a) and ZBNR (b)

To further understand the essence of deformation in different phases of in-plane tensile strain, we have analyzed the bond (E_B) and angle energy (E_A) (see Fig. 7). By comparing Fig. 6 and Fig. 7, and combining with Fig. 4 and Fig. 5, it isn't difficult to find that deformation features of ABNR and ZBNR are entirely different. The deformation process for the ABNR can be divided into four typical stages: the linear elasticity, elastic-plastic, plastic and fracture phases, but the deformation process for the ZBNR is simpler, almost straight from the linear elasticity to fracture. Fig. 6 and 7 show that the changes of the bond stretching and angle bending are the main factors that influence deformation, specially the former, among which the dominating factors are structural deformation of stretched BNRs. Fig. 6 shows the critical elastic strains of ABNR and ZBNR are 15.30% and 22.03%, respectively. Obviously, the critical elastic strains of ZBNRs are significantly greater than ABNRs.

In addition, comparing Fig.6 and Fig.7, one can find that the total energy E_T is mainly contributed by E_B and E_A. Also, E_A is much larger than E_B, which indicates that E_A dominates the E_T. The main reasons are as follows: in the equation (1), the bond stretching $E_B = \sum_{bonds} \frac{1}{2} k_r (r - r_0)^2$ and the angle bending $E_A = \sum_{angles} \frac{1}{2} k_\theta (\theta - \theta_0)^2$, where $r - r_0$ and $\theta - \theta_0$ are deviations of bond length or angle from equilibrium. Due to the special atomic configuration of borophene, the most bond direction are not entirely tensile direction, the most of bond length deviations $r - r_0$ is almost very small only when applying the strains on borophene are not too great. In particular, almost all of bond length maintain equilibrium length without the strain, their deviations $r - r_0$ are close to zero. However, $\theta - \theta_0$ is different, because the all bond angle θ in borophene under unideal situation is more difficult to maintain their consistency, especially many hexagonal hole defects in borophene. Consequently, E_A is much larger than E_B. In the expression of E_T, the contribution of latter terms generally are little and the E_T is mainly contributed by the first two terms E_B and E_A under in-plane tensile strains in this paper.

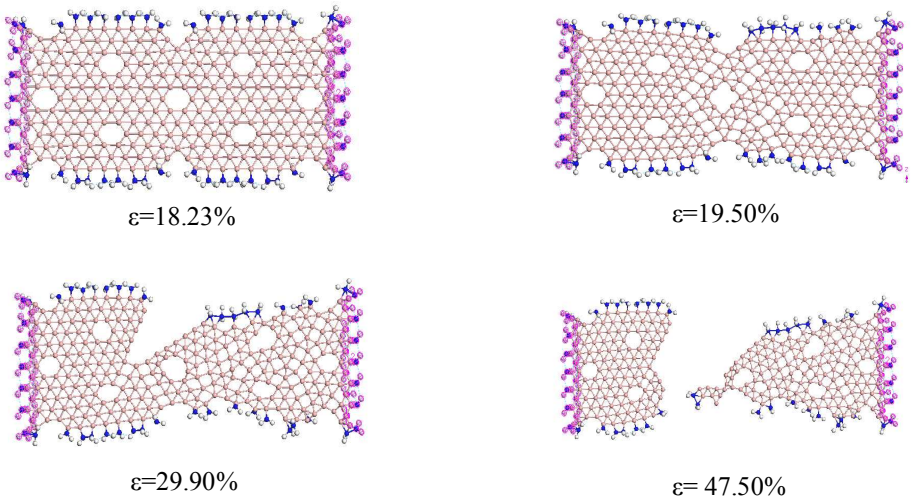

Fig. 8 Geometric structure of ABNR-NH_2 with different in-plane tensile strains ε

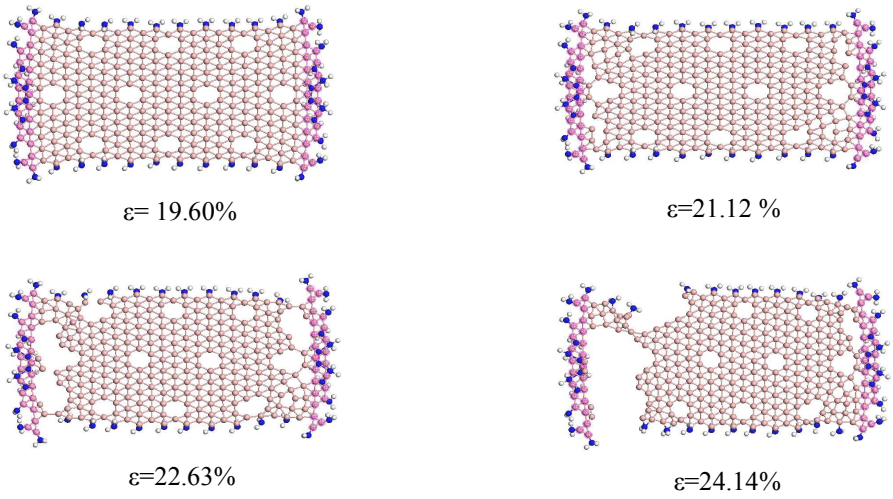

Fig. 9 Geometric structure of ZBNR-NH_2 with different in-plane tensile strains ε

When grafted around nanoribbons with amine groups, some changes occur in all of the above structural properties of BNR-NH_2 under different in-plane tensile strains. Fig. 8 and 9 show geometric structure changing process of grafted ABNRs and ZBNRs. The results show that the bond-breaking strain in internal hexagonal vacancies at the center increase from 16.7% to 19.5% for ABNR, while the strain for no distortion in ZBNR decreases slightly from 22.0% to 21.1%. In particular, when the strain occurs on BNR, cracks obviously increase from 26.9% to 29.9% for ABNR and from 24.1% to 22.6% for ZBNR. The structural fracture modes for grafted BNR still remain similar to the aforementioned non-grafted BNR.

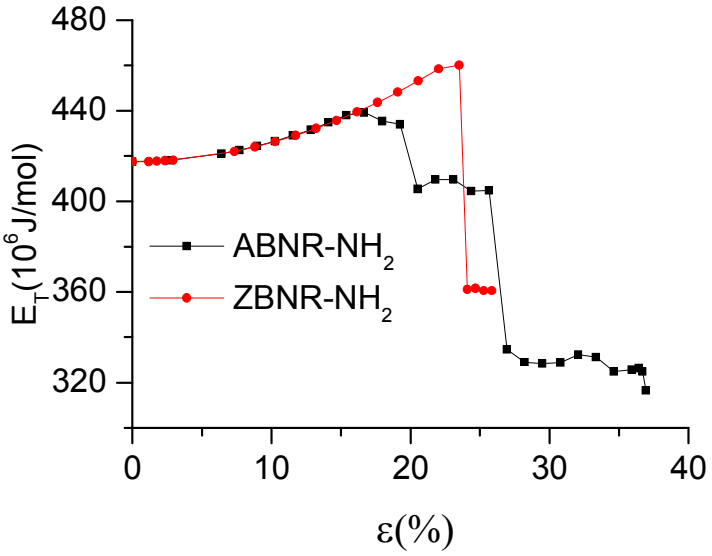

Fig. 10 Effect of different in-plane tensile strains (ε) on the total potential energy (E_T) of BNR-NH_2

The effects of different in-plane tensile strains (ε) on the total potential energy (E_T) of grafted ABNR and ZBNR are as shown in Fig. 10. By comparing Fig. 6 and Fig. 10, it's easy to see that the grafted ABNR and ZBNR still have distinctly different elastic strain ranges and slightly different elastic modules, as is the case with non-grafted BNR. By fitting the curve around the equilibrium position, their elastic coefficients can be calculated. Through further data fitting, the functional correlation between the total potential energy and strain around the equilibrium position can be obtained as follows:

$$E_T = 416.17487 - 0.01245\varepsilon + 895.45165\varepsilon^2 \quad \text{for ABNR-NH}_2 \tag{5}$$

$$E_T = 416.22776 - 0.83926\varepsilon + 878.22102\varepsilon^2 \quad \text{for ZBNR-NH}_2 \tag{6}$$

Based on Formula (2), combined with Formulae (5) and (6), the Young's moduli for grafted ABNRs and ZBNRs have been computed. The results indicate that the Young's moduli for ABNR-NH_2 and ZBNR-NH_2 are 1.125 *TPa* and 1.016 *TPa*, respectively. The

moduli for armchair are still larger than for zigzag, and both are greater than non-grafted BNR. Besides, the modulus ratio of armchair to zigzag (Ya /Yz) reduces slightly from 1.117 to 1.107, showing that the anisotropy of in-plane elastic property of BNR improves somewhat with grafted amine groups. In particular, with grafting, the critical elastic strains of ABNR-NH_2 and ZBNR-NH_2 are increased to 18.2%s and 21.12%. Similar to the aforementioned non-grafted BNR, the former are still greater than the latter.

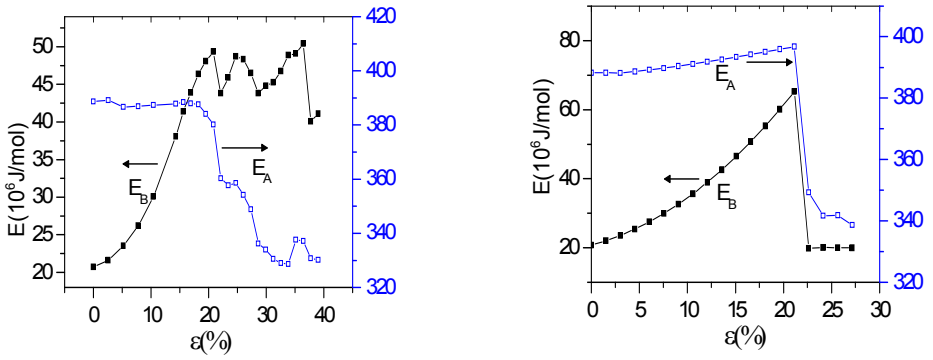

(a) ABNR-NH_2 （b）ZBNR-NH_2

Fig. 11 Effect of different in-plane tensile strain (ε) on the bond (E_B) and angle energy (E_A) of the arm (a) and zig BNR-NH_2 (b)

Fig. 11 further shows the bond (E_B) and angle energy (E_A) of the ABNR-NH_2 and ZBNR-NH_2 with different in-plane tensile strains. Compared with non-grafted BNR, it can be found that the strains at which E_B suddenly fall significantly increases for ABNR (from 25.65% to 36.45%) and decreases for ZBNR (from 23.51% to 21.12%). This is consistent with the above-mentioned structural evolution and the E_T change. The results indicate that the main reason for the obvious crack in BNR is bond tolerance; grafting amine groups is

useful for strengthening crack resistance of armchair but not zigzag.

To better understand the relationship between differences in elasticity of the aforementioned BNRs and their structures, we further investigated their radial distribution functions (RDFs). The $g(r)$ in RDFs gives the probability of finding a B atom in the distance r from another reference B atom. If we count the appearance of two B atoms at separation r, from $r = 0$ to $r = \infty$, we can get the radial distribution function $g(r)$. To quantify the crystalline perfection of BNRs under the different circumstances, we have computed the distribution of the inter-atomic distances from the atomic coordinates ($g(r)$) by using molecular dynamics. The RDF is a useful tool for describing the structure of a system. In a solid, it exhibits a number of sharp peaks, separations and heights characteristic of a lattice structure. In RDFs of BNR nanosheets, peak locations (abscissa values) correspond to the distance between the first, second and other neighboring atoms separation from reference atom on the sheet. The ordinate values for peaks represent that it is relative probability that two B atoms would be found at this separation. To calculate the pair distribution function from a simulation, the neighbors around each atom or molecule are sorted into distance bins. The number of neighbors in each bin is averaged over the entire simulation. For example, a count is made of the number of neighbors for every atom or molecule in the simulation. This count can be performed during the simulation itself or by analyzing the configurations that are generated, so based on analysis to the optimized structures, the RDF can be directly obtained from molecular dynamics simulation. The FWHM can be got by calculating the abscissa difference values at half maximum ordinate values for peaks in RDF**.** In general, the full width at half maximum (FWHM) of an RDF is closely related to the integrity of the crystal structure. The more integrated the structure is, the sharper the RDF peaks are and the smaller the FWHM is, and vice versa.

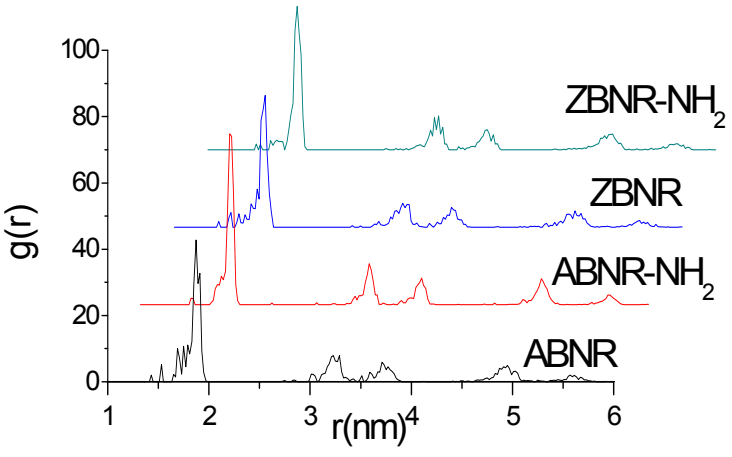

Fig. 12 RDF of grafted and non-grafted BNRs.

Table 1 Main peak positions and FWHMs of RDF (nm)

Materials	First peak		Second peak		Third peak	
	Location	FWHM	Location	FWHM	Location	FWHM
ABNR	0.186	0.0802	0.323	0.1410	0.371	0.1235
ABNR-NH_2	0.186	0.0750	0.323	0.0907	0.371	0.1162
ZBNR	0.186	0.0773	0.323	0.1450	0.371	0.1080
ZBNR-NH_2	0.186	0.0760	0.323	0.1380	0.371	0.1078

Fig. 12 (Table 1) shows that there is some difference between RDF parameters in grafted and non-grafted BNRs. Locations of their highest peaks, subpeaks and third peaks are about 0.186, 0.323 and 0.371nm, respectively, with little significant change taking place among the BNRs. But their FWHMs are different. The first three FWHMs for ABNR are about 0.0802, 0.1410 and 0.1235nm, respectively. After being grafted, the FWHMs are 0.0750, 0.0907 and

0.1162nm. It can be seen that the FWHMs for grafted BNRs are slightly smaller than those for non-grafted BNRs. Similarly, the FWHMs of the first three peaks for ZBNR are about 0.0773, 0.1450 and 0.1080nm, respectively. After grafting, the FWHMs are 0.0760, 0.1380 and 0.1078nm. FWHMs for grafted BNRs are still slightly smaller than those for non-grafted BNRs. These results can be attributed to the differences in free boundary shapes and grafts and lead to the differences between B-B bond lengths of BNRs in the triangular lattices. These results indicate that grafts can decrease the FWHMs of the crystal structure, thereby improving the integrity of the crystal structure. Comparison of the FWHMs in terms of the elastic moduli, the critical elastic strains and the rupture strains before and after grafting shows that the elastic properties of BNRs are basically related to the integrity of the crystal structure. The smaller the FWHMs are, the more integrated the structure is and the stronger the distortion resistance is.

3.2. High-temperature structural stability of BNRs

As with graphene, BNR and its composite structures are likely to be used in varying high-temperature environments in actual applications, such as the spark plasma sintering of graphene reinforced zirconium diboride ultra-high temperature ceramic composites,[45] high-temperature multifunctional magneto active nickel graphene polyamide nanocomposites,[46] and so on. In order to know the high-temperature structural stability of BNRs, structural performances of the above-mentioned four BNRs, when subjected to high temperatures, are simulated and analysed through molecular dynamics simulations. Fig. 13 shows the overall appearance of the four BNRs after quenching at temperature of 1500 K.

Because the difference at lower quenching temperature is not large enough to clearly describe, a higher quenching temperature (1500 K) is selected in this paper. It is evident that the structural deformation in Fig. 13a1 and a2 is obviously greater than that in Fig. 13b1 and b2. In the former, some areas of the structures exhibit some chaos in bond orders and the hexagonal holes in the structures are obviously distorted or ambiguous, whereas those in the latter display only slight chaos in bond orders and no obvious distortions, especially near the clear hexagonal holes in the structures. At the same time, comparison of Fig. 6 (a1) and (a2) shows that deformation of zigzag is slightly less than that of armchair BNR but Fig. 6b1 and b2 show no evident difference between the armchair and the zigzag in terms of structural deformation. This indicates that the degree of structure distortion is related to the chirality, i.e. there is some thermal expansion anisotropy in BNR. Therefore, grafted amine groups can not only enhance resistance to deformation at high temperature but also reduce its thermal expansion anisotropy. The geometric models of BNRs at high temperature suggest that grafted amine groups have certain protective effects that improve the high temperature structural stability of BNRs.

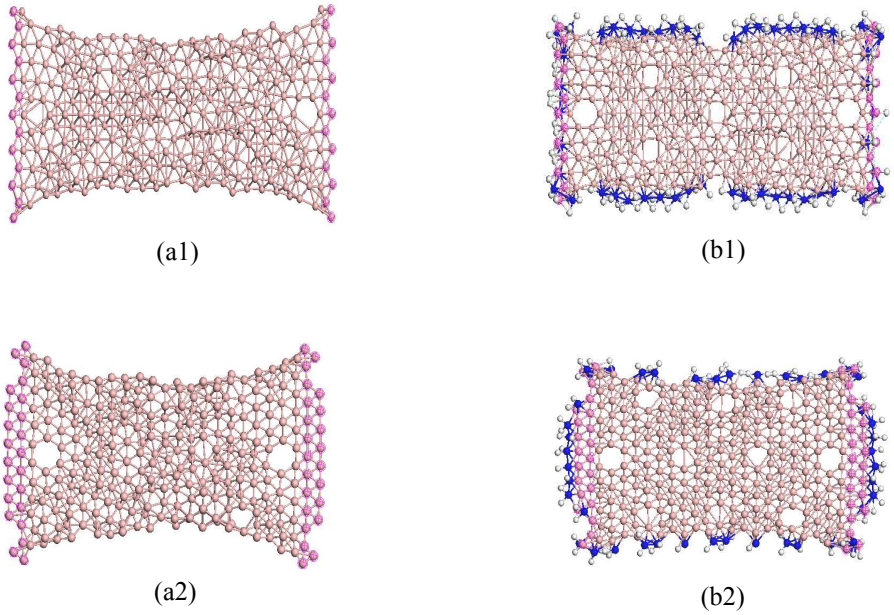

Fig. 13 Geometric models of ABNR and ZBNR (a1, a2) and ABNR-NH_2 and ZBNR-NH_2 (b1, b2) after quenching at 1500 K.

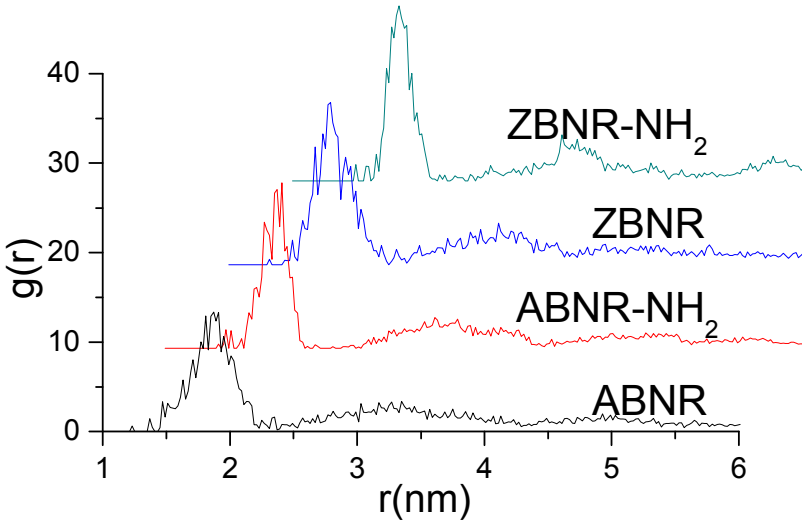

Fig. 14 RDF of grafted and non-grafted BNRs after quenching at 1500K.

Table 2 FWHMs (nm) of the first RDF peak for grafted and non-grafted BNRs after quenching at a temperature of 1500K

Material	FWHM	Material	FWHM
ABNR	0.03558	ABNR-NH_2	0.02165
ZBNR	0.03094	ZBBR-NH_2	0.02011

Fig. 14 (Table 2) shows RDF parameters at quenching temperature of 1500K. The thermal expansion of atomic distances and the increases of lattice vibrational frequency occur with the rise of temperature based on the basis of thermodynamics, so it is reasonable that RDF values of grafted and non-grafted BNRs after quenching at 1500 K (Fig. 14) have more noise than data presented in Fig. 12. From Fig. 14 (Table 2), the FWHMs of the highest peaks for ABNR and ZBNR are 0.03558 and 0.03094nm, respectively. When grafted, distribution of the peak narrows. FWHM of the highest peak for ABNR decreases from 0.03558 to 0.02165 nm and that for ZBNR decreases from 0.03094 to 0.02011nm. These results indicate that at a high temperature, the structure displays smaller deviation in distance. The neighbouring atomic distances are more concentrated at all levels in the triangular lattices on nanosheets. Hence, crystal structures of BNRs are protected by the amine grafts to a certain extent, suggesting that BNR-NH_2 has higher resistance to distortion at high temperature. Therefore, grafting amine groups can improve the structural stability of BNRs at high temperature. In addition, it's easy to find that FWHM of the ABNR is greater than ZBNR but that of grafted ABNR is closer to that of grafted ZBNR. This result indicates that

grafting amine groups effectively reduces the thermal expansion anisotropy of BNR. The RDF quantitative analysis result is consistent with the above-mentioned geometric shapes.

4. Conclusions

The molecular dynamics simulations suggest that Young's moduli of ABNR are slightly greater than those of ZBNR. Grafting amine groups can increase moduli and decrease some anisotropy of elastic moduli. Optimizing the structures of BNRs and BNRs-NH_2 with different in-plane tensile strains shows that the critical elastic strain for ABNR is less than ZBNR and grafting amine groups can increase the strain. However, the ZBNR is somewhat different as grafting amine groups slightly reduces the strain. The result indicates that grafting amine groups can enhance elastic strain range of ABNR and efficiently reduce the anisotropy of elastic strain for BNR. Their fracture modes are completely different; ABNR and ZBNR show distinct typical ductile and brittle fractures, respectively. The crack for ABNR begins from the middle and that for ZBNR begins from both ends. The deformation process for the ABNR has four distinct stages: the linear elasticity, elastic-plastic, plastic and fracture phases, and the breakup of ZBNR occurs so fast that one is unable to see the transitional processes. The analysis results for failure strain indicate that the main reason of obvious cracking of BNR is bond tolerance; grafting amine groups is useful for strengthening the crack resistance of armchair but not zigzag. Geometric structures of the BNRs and BNRs-NH_2 at quenching temperature of 1500K show that the deformation of the armchair is slightly greater than that for the zigzag, but grafted amine groups can significantly strengthen the capacity to resist deformation at high temperature and reduce the

thermal expansion anisotropy. The analysis results for RDF reveal that elastic properties, anti-deformability and high temperature structural stability of BNR have some corresponding correlations with their crystallinities.

Acknowledgements

The work described in this paper was supported by grants from the Research Grants Council of the Hong Kong Special Administrative Region, China (Project No. 9042047, CityU 11208914) and National Natural Science Foundation of China (Grant No. 51378448). The work was also supported by Hunan Provincial Natural Science Foundation of China (Project No. 14JJ2076), Aid Program for Teaching Reform Project of Changsha University of Science and Technology (Project No. JG1323), the Construct Program of the Key Discipline in Hunan Province and Aid Program for Science and the Technology Innovative Research Team in Higher Educational Institutions of Hunan Province, China.

References

1. A. K. Geim, *Science*, 2009, 324, 1530-1534.
2. Z. A. Piazza, H. S. Hu, W. L. Li, Y. F. Zhao, J. Li and L. S. Wang, *Nat. Commun.*, 2014, 5, 3113.
3. W. L. Li, Q. Chen, W. J. Tian, H. Bai, Y. F. Zhao, H. S. Hu, J. Li, H. J. Zhai, S. D. Li and L. S. Wang, *J. Am. Chem. Soc.*, 2014, 136, 12257-12260.
4. A. Chavez-Valdez, M. S. P. Shaffer and A. R. Boccaccini, *J. Phys. Chem. B*, 2013, 117, 1502-1515.
5. L. Xiaoyang, L. Peng, W. Yang, L. Qunqing, W. Jiaping, W. Yang, F. Chen, Z. Lina, F. Shoushan and J. Kaili, *Nat. Commun.*, 2013, 4, 2920.
6. W. L. Li, Y. F. Zhao, H. S. Hu, J. Li and L. S. Wang, *Angew. Chem.-Int. Edit.*, 2014, 53, 5540-5545.
7. Q. Chen, G. F. Wei, W. J. Tian, H. Bai, Z. P. Liu, H. J. Zhai and S. D. Li, *Phys. Chem. Chem. Phys.*, 2014, 16, 18282-18287.
8. I. A. Popov, Z. A. Piazza, W.-L. Li, L.-S. Wang and A. I. Boldyrev, *J. chem. phys.*, 2013, 139, 144307.

9. W. Huang, A. P. Sergeeva, H. J. Zhai, B. B. Averkiev, L. S. Wang and A. I. Boldyrev, *Nat. Chem.*, 2010, 2, 202-206.
10. I. Boustani, *Phys. Rev. B*, 1997, 55, 16426-16438.
11. F. Li, P. Jin, D. E. Jiang, L. Wang, S. B. Zhang, J. Zhao and Z. Chen, *J. Chem. Phys*, 2012, 136, 074302.
12. S. De, A. Willand, M. Amsler, P. Pochet, L. Genovese and S. Goedecker, *Phys. Rev. Lett.*, 2011, 106, 225502.
13. I. Boustani, A. Quandt, E. Hernandez and A. Rubio, *J. Chem. Phys.*, 1999, 110, 3176-3185.
14. J. Kunstmann and A. Quandt, *Phys. Rev. B*, 2006, 74, 035413.
15. H. Tang and S. Ismail-Beigi, *Phys. Rev. B*, 2010, 82, 115412.
16. Y. Ding, X. Yang and J. Ni, *Appl. Phys. Lett.*, 2008, 93, 043107.
17. T. R. Galeev, Q. Chen, J. C. Guo, H. Bai, C. Q. Miao, H. G. Lu, A. P. Sergeeva, S. D. Li and A. I. Boldyrev, *Phys. Chem. Chem. Phys.*, 2011, 13, 11575-11578.
18. E. S. Penev, S. Bhowmick, A. Sadrzadeh and B. I. Yakobson, *Nano Lett.*, 2012, 12, 2441-2445.
19. H. G. Lu, Y. W. Mu, H. Bai, Q. Chen and S. D. Li, *J. Chem. Phys.*, 2013, 138, 024701.
20. S. Banerjee, G. Periyasamy and S. K. Pati, *J. Mater. Chem. A*, 2014, 2, 3856-3864.
21. Y. Y. Liu, E. S. Penev and B. I. Yakobson, *Angew. Chem.-Int. Edit.*, 2013, 52, 3156-3159.
22. H. Tang and S. Ismail-Beigi, *Phy. Rev. Lett.*, 2007, 99, 115501.
23. X. B. Yang, Y. Ding and J. Ni, *Phys. Rev. B*, 2008, 77, 041402.
24. X. J. Wu, J. Dai, Y. Zhao, Z. W. Zhuo, J. L. Yang and X. C. Zeng, *Acs Nano*, 2012, 6, 7443-7453.
25. H. Tang and S. Ismail-Beigi, *Phys. Rev. B*, 2009, 80, 134113.
26. S. Er, G. A. de Wijs and G. Brocks, *J. Phys. Chem. C*, 2009, 113, 18962-18967.
27. A. Hansson, M. Paulsson and S. Stafstrom, *Phys. Rev. B*, 2000, 62, 7639-7644.
28. D. Yu and F. Liu, *Nano Lett.*, 2007, 7, 3046-3050.
29. F. Schedin, A. K. Geim, S. V. Morozov, E. W. Hill, P. Blake, M. I. Katsnelson and K. S. Novoselov, *Nat. Mater.*, 2007, 6, 652-655.
30. J. H. Yuan and K. M. Liew, *Carbon*, 2009, 47, 713-721.
31. N. Yuxiang, J. Jiechao, E. Meletis and T. Dumitrica, *Appl. Phys. Lett.*, 2015, 107, 031603.
32. K. M. Liew and J. H. Yuan, *Nanotechnology*, 2011, 22, 085701.
33. J. H. Yuan and K. M. Liew, *Phys. Chem. Chem. Phys.*, 2014, 16, 88-94.
34. A. Montazeri, S. Ebrahimi and H. Rafii-Tabar, *Mol. Simul.*, 2015, 41, 1212-1218.
35. R. Konnola, J. Joji, J. Parameswaranpillai and K. Joseph, *RSC Adv.*, 2015, 5, 61775-61786.
36. A. K. Rappe, C. J. Casewit, K. S. Colwell, W. A. Goddard and W. M. Skiff, *J. Am. Chem. Soc.*,1992, 114, 10024-10035.
37. N. Yao and V. Lordi, *J. App. Phys.*, 1998, 84, 1939-1943.
38. C. J. Casewit, K. S. Colwell and A. K. Rappe, *J. Am. Chem. Soc.*, 1992, 114, 10035-10046.
39. L. Boldrin, F. Scarpa, R. Chowdhury and S. Adhikari, *Nanotechnology*, 2011, 22,

505702.
40. C. Lee, X. D. Wei, J. W. Kysar and J. Hone, *Science*, 2008, 321, 385-388.
41. Z. H. Ni, H. M. Wang, J. Kasim, H. M. Fan, T. Yu, Y. H. Wu, Y. P. Feng and Z. X. Shen, *Nano Lett.*, 2007, 7, 2758-2763.
42. M. S. Dresselhaus, G. Dresselhaus and P. C. Eklund, *Science of fullerenes and carbon nanotubes*, Academic Press, San Diego, 1996.
43. E. Konstantinova, S. O. Dantas and P. Barone, *Physical Review B*, 2006, 74, 035417.
44. H. Zhao, K. Min and N. R. Aluru, *Nano Lett.*, 2009, 9, 3012-3015.
45. G. B. Yadhukulakrishnan, S. Karumuri, A. Rahman, R. P. Singh, A. K. Kalkan and S. P. Harimkar, *Ceram. Int.*, 2013, 39, 6637-6646.
46. M Yoonessi, D. A. Scheiman, M. Dittler, J. A. Peck, J. Ilavsky, J. R. Gaier and M. A. Meador, *Polymer*, 2013, 54, 2776-2784.